

Orbital and Charge Excitations as Fingerprints of an Orbital-Selective Mott Phase in the Block Magnetic State of BaFe₂Se₃

N. D. Patel,^{1,2} A. Nocera,^{1,2} G. Alvarez,³ A. Moreo,^{1,2} S. Johnston,^{1,4} and E. Dagotto^{1,2}

¹*Department of Physics and Astronomy, The University of Tennessee, Knoxville, Tennessee 37996, USA*

²*Materials Science and Technology Division, Oak Ridge National Laboratory, Oak Ridge, Tennessee 37831, USA*

³*Computer Science & Mathematics Division and Center for Nanophase Materials Sciences, Oak Ridge National Laboratory, Oak Ridge, Tennessee 37831, USA*

⁴*Joint Institute for Advanced Materials at The University of Tennessee, Knoxville, Tennessee 37996, USA*

Resonant inelastic x-ray scattering (RIXS) applied to the ladder BaFe₂Se₃ unveiled an exotic two-peak structure [Phys. Rev. B **88**, 165103 (2013)], associated with local orbital (*dd*) excitations in a block-type antiferromagnetic phase. A mixed character between band and correlated materials was reported. Here, using the density matrix renormalization group method, we calculate the momentum-resolved charge- and orbital-dynamical response functions of a multi-orbital Hubbard model. Remarkably, our results qualitatively resemble the BaFe₂Se₃ RIXS data only when the studied model is in an orbital-selective Mott phase (OSMP). The zero-momentum transfer RIXS peaks correspond to excitations between itinerant and Mott insulating orbitals. Our predicted momentum-resolved charge and orbital dynamical structure factors can provide further insight in the predicted OSMP regime of BaFe₂Se₃.

Introduction — The discovery of superconductivity in the two-leg ladder compounds BaFe₂S₃ [1, 2] and BaFe₂Se₃ [3] opened a new branch of research: these are the first members of the iron superconductors family [4–6] without iron layers, the parent compounds are insulators [1, 2], and low-dimensionality allows for accurate theoretical treatment [7–11]. For this reason, iron-ladder compounds have been the focus of many theoretical and experimental studies [1–3, 12–21]. In particular, inelastic neutron scattering data [19] is compatible with the exciting idea that ambient pressure BaFe₂Se₃ is in an orbital selective Mott phase (OSMP) [22–24] with an exotic 2×2 block antiferromagnetic (AFM) order, where one orbital is localized with a Mott gap while the others are gapless and itinerant. Resonant inelastic x-ray scattering (RIXS) and x-ray photoemission (XPS) experiments report the presence of both localized and itinerant carriers in BaFe₂Se₃, also suggesting OSMP physics [20, 21]. However, at present there is no sufficient theoretical evidence supporting these (indirect) claims of an OSMP ground state in BaFe₂Se₃.

The first step towards understanding the characteristic excitations of an OSMP is to calculate its single particle spectra $A(\mathbf{k}, \omega)$ and its intra- and inter-orbital dynamical spin $S(\mathbf{q}, \omega)$, charge $N(\mathbf{q}, \omega)$, and orbital $L(\mathbf{q}, \omega)$ structure factors. Recently, the theoretical predictions for $A(\mathbf{k}, \omega)$ and $S(\mathbf{q}, \omega)$ were presented [25, 26] in a block AFM OSMP. However, $N(\mathbf{q}, \omega)$ and $L(\mathbf{q}, \omega)$, crucial for RIXS experiments, have not been addressed yet. Here, we use density matrix renormalization group (DMRG) to compute the momentum-resolved charge and orbital response functions for the magnetic block OSMP of a multi-orbital Hubbard chain for the first time. We compare our results against RIXS data for BaFe₂Se₃ [20], which measures charge, orbital, and magnetic excitations simultaneously [27–31]. By calculating the orbital re-

sponse functions of competing paramagnetic metal (PM) and ferromagnetic (FM) insulator states, we show that block OSMP has a characteristic two-peak structure that is distinctive and in striking agreement with RIXS results on BaFe₂Se₃ [20]. Moreover, we identify the observed *dd* peaks as orbital excitations between localized and itinerant orbitals within the OSMP. Our results strongly suggest that the ground state of BaFe₂Se₃ is indeed an OSMP with block magnetic order.

Model — We use a multi-orbital Hubbard model composed of kinetic energy and interaction terms as $H = H_K + H_I$. The kinetic energy part of the Hamiltonian is

$$H_K = \sum_{i,\sigma,\gamma,\gamma'} t^{\gamma\gamma'} (c_{i\gamma\sigma}^\dagger c_{i+1\gamma'\sigma} + \text{H.c.}) + \sum_{i,\sigma,\gamma} \epsilon_\gamma n_{i\sigma\gamma},$$

where $c_{i\gamma\sigma}^\dagger$ ($c_{i\gamma\sigma}$) creates (destroys) an electron at site i , orbital γ , and spin σ . The first term represents nearest-neighbor electron hopping from orbital γ' to γ with a hopping amplitude $t^{\gamma\gamma'}$. We denote the relevant orbitals d_{xz} , d_{yz} , and d_{xy} as a , b , and c , respectively. The second term contains the orbital-dependent crystal field splitting. The parameters are (eV units) $\epsilon_a = -0.1$, $\epsilon_b = 0.0$, $\epsilon_c = 0.8$, $t^{aa} = t^{bb} = 0.5$, $t^{cc} = 0.15$, and $t^{ac} = t^{bc} = t^{ca} = t^{cb} = -0.10$. The non-interacting bandwidth is $W = 4.9t^{aa}$. This set of parameters is known [24] to produce bands that emulate iron-based superconductors, with hole pockets at $k = 0$ and an electron pocket at $k = \pm\pi$ [5]. Our reported results are all at zero temperature.

The interaction term, in standard notation, is

$$H_I = U \sum_{i,\gamma} n_{i\gamma\uparrow} n_{i\gamma\downarrow} + (U' - \frac{J_H}{2}) \sum_{i,\gamma < \gamma'} n_{i\gamma} n_{i\gamma'} - 2J_H \sum_{i,\gamma < \gamma'} \mathbf{S}_{i\gamma} \cdot \mathbf{S}_{i\gamma'} + J_H \sum_{i,\gamma < \gamma'} (P_{i\gamma}^\dagger P_{i\gamma'} + \text{H.c.}).$$

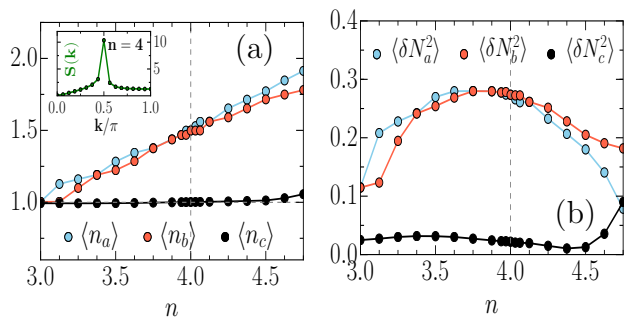


FIG. 1. (color online) (a) Average local occupation of each orbital vs. overall electron density n , where $n = 4$ represents the filling of 4 electrons per site (using DMRG, 32 sites). The inset shows the total spin structure factor with a peak at $k = \pi/2$, representing the block type AFM order at $n = 4$. (b) Average local charge fluctuations on each orbital vs. n .

The first term is the intraorbital Hubbard repulsion U . The second is the interorbital repulsion between electrons at different orbitals, with $U' = U - 2J_H$. The third term is the Hund's coupling J_H , and the last term represents the on-site interorbital hopping of electron pairs. Explicit definitions for all the operators in the model are in the supplementary material [32]. The rich physical properties realized by this model were discussed extensively in Ref. [24]. Most of the data presented here was gathered at $J_H/U = 0.25$ (as used extensively before [24, 33, 34]) and $U/W = 0.8$ where the block-type AFM OSMP is known to be stable [24]. However, we also show results for the paramagnetic metal (PM, small U) and ferromagnetic insulator (FM, large U) phases to highlight unique features of the block OSMP by contrast.

Observables — To characterize the OSMP, we calculate the dynamical response functions

$$O(i, j, \omega) = \frac{-1}{\pi} \text{Im} \left[\langle \psi_0 | O_i^\dagger \frac{1}{\omega - H + E_g + i\eta} O_j | \psi_0 \rangle \right] \quad (1)$$

using DMRG within the correction-vector formulation in Krylov space [35, 36]. The single-particle spectral function is obtained using $O_i = c_{i\sigma\gamma}$. The intraorbital particle-hole (charge) excitations arise using $O_i = \sum_\sigma n_{i\sigma\gamma} - \langle n_{i\sigma\gamma} \rangle$, where we explicitly subtract the ground-state contribution to measure only the fluctuations. Finally, the orbital excitations are obtained using $O_i = \{L_i^x, L_i^y, L_i^z\}$, where $L_i^x = i \sum_\sigma (c_{ia\sigma}^\dagger c_{ic\sigma} - c_{ic\sigma}^\dagger c_{ia\sigma})$, $L_i^y = i \sum_\sigma (c_{ib\sigma}^\dagger c_{ic\sigma} - c_{ic\sigma}^\dagger c_{ib\sigma})$, and $L_i^z = i \sum_\sigma (c_{ia\sigma}^\dagger c_{ib\sigma} - c_{ib\sigma}^\dagger c_{ia\sigma})$. These operators are derived from the $L = 2$ angular momentum operators in the t_{2g} orbital basis [32].

Results — Figure 1a demonstrates that the OSMP is robust against hole and electron doping [37]. The local charge occupation (panel a) and fluctuations (panel b) of each orbital vs. the total electronic density are shown. First, we focus on the results for 4 electrons per site ($n = 4$), shown by the vertical dashed line in Fig. 1 (note that $n = 4$ in a three-orbital model is the analog of $n = 6$ in a five-orbital model). At this density,

orbital c has one electron per site while the other two orbitals remain fractionally occupied. The corresponding intra-orbital charge fluctuations $\langle \delta N_\gamma^2 \rangle = \langle n_\gamma^2 \rangle - \langle n_\gamma \rangle^2$ in orbital c are significantly suppressed, but charge fluctuations in orbitals a and b remain finite at $n = 4$. Additionally, the inset of Fig. 1a contains the spin structure factor at $n = 4$, displaying the characteristic peak at $k = \pi/2$ in agreement with the experimentally observed non-trivial block-type AFM order. It is important to note that orbital c (d_{xy}) has the standard characteristics of a Mott phase at $n = 4$, where charge degrees of freedom are “frozen” (localized) accompanied by well-formed local magnetic moments, $\mathbf{m}_c \sim 0.98\mu_B$. However, large local charge fluctuations of the other orbitals suggests a metallic behavior typical of itinerant electrons. The total on-site local moment at $n = 4$ is $\mathbf{m}_{tot} \simeq 1.97\mu_B$, a robust value slightly larger than in experiments [13, 15, 19].

The coexistence of localized and itinerant carriers is also evident when examining the electronic density of each orbital vs. global filling (Fig. 1a). The linear behavior of n_a and n_b suggests a band-like picture, while the plateau in n_c over a range of doping ($n = [3 : 4.5]$) indicates the presence of a Mott gap in the single-particle spectrum of orbital c . Since we correctly capture the magnetic properties of BaFe_2Se_3 at $n = 4$, henceforth we fix the filling $n = 4$ to probe block OSMP excitations.

Figures 2a and 2b show the orbital-resolved single-particle spectra. Orbitals a and b have a finite quasi-particle weight at E_F , as also shown in the density-of-states in Figure 3a, confirming the itinerant nature of electrons in these orbitals. Moreover, we find that orbital c has a gap of $\Delta_c \sim 1.5$ eV [38] in $A^c(k, \omega)$ (Figs. 2b and 3a), compatible with our analysis in Figs. 1a and 1b. The single-particle spectra clearly demonstrate the coexistence of gapped Mott (localized) and gapless itinerant carriers and agree with earlier studies of a similar model [25]. Note also the presence of a pseudogap in the itinerant $d_{xz/yz}$ orbitals, resulting from proximity to the PM Hund metal phase [39] (Fig. 3a).

To arrive to our main conclusions, we now calculate the charge (Figs. 2c and 2d) and orbital (Figs. 2e and 2f) dynamics of the block-AFM OSMP. Similarly as in $A^c(k, \omega)$, the charge excitations of the Mott orbital c display a gap $\Delta_c^N \sim 1.5$ eV (Fig. 2d). The excitations of the itinerant orbitals display instead a *gapless* continuum (Fig. 2c) because charge fluctuations can propagate freely in a metallic system. Additionally, $N^c(k, \omega)$ is dispersion-less, indicating that these high-energy states are localized, compatible with doubly occupied orbitals d_{xy} with an energy proportional to the Mott gap. Contrast our results with the one-orbital two-leg ladder Hubbard model where charge excitations are gapped in the half-filled Mott phase, but display a gapless continuum in the metallic phase away from half-filling [40]. Our results show the *simultaneous* presence of localized and itinerant fermions in our multi-orbital model.

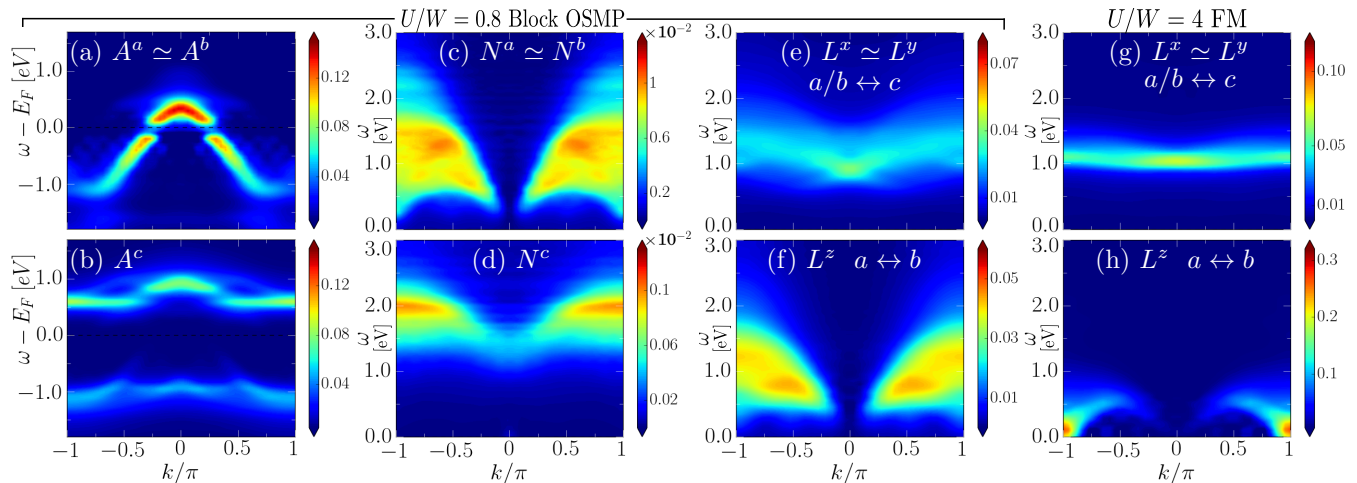


FIG. 2. (color online) Orbital-resolved (a-b) single-particle spectra, (c-d) charge excitations, and (e-f) orbital excitations spectra within the block AFM OSMP. $A^{a/b}(k, \omega)$ has reduced but nonzero quasi-particle weight at the Fermi level (E_F) while $A^c(k, \omega)$ has a Mott gap $\Delta_c \sim 1.5$ eV. The charge excitations $N^{a/b}(k, \omega)$ have a gapless continuum at finite ω while $N^c(k, \omega)$ has an excitation gap of $\Delta_c^N \sim 1.5$ eV. $L^{x/y}(k, \omega)$ represent inter-orbital excitations between orbitals a/b and c ($d_{xz/yz} \leftrightarrow d_{xy}$) that are gapped with an excitation gap $\Delta^L \sim 0.7$ - 0.9 eV. $L^z(k, \omega)$ are inter-orbital excitations between orbitals a and b ($d_{xz} \leftrightarrow d_{yz}$). (g-h) orbital excitations spectra within the FM insulator where $L^{x/y}(k, \omega)$ has a gap ~ 0.9 eV and $L^z(k, \omega)$ is gapless with a robust $k = \pi$ peak indicating quasi-long range staggered orbital ordering in the FM phase. Spectral functions are calculated using $\Delta\omega = 0.05$ eV, broadening $\eta = 0.1$ eV, up to 1200 DMRG states, 24 sites (a-d), 16 sites (e-h), and 8 sweeps.

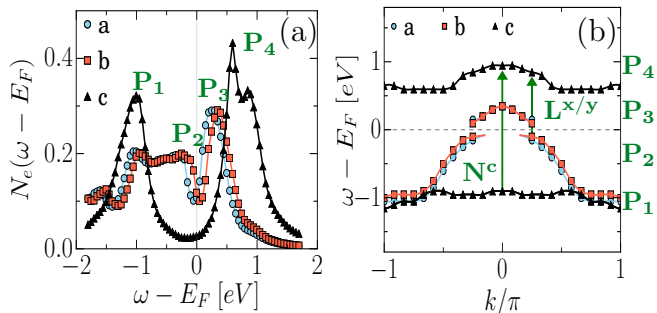


FIG. 3. (color online) Orbital-resolved (a) density of states, and (b) poles of the total single-particle spectra (Figs. 2a and 2b) of the block AFM OSMP (using DMRG with 24 sites).

Consider now the k -resolved orbital excitations in the block OSMP. Figure 2e ($L^{x/y}(k, \omega)$) shows the excitations from (to) itinerant orbitals a/b to (from) localized orbital c . Figure 2f displays a gapless continuum in orbital excitations, $L^z(k, \omega)$, between the itinerant orbitals a and b . These dynamical spectra can be understood using the density-of-states (Fig. 3a), and poles of the single-particle states of the OSMP (Fig. 3b). Figure 3a shows that electron scattering from $P_2 \rightarrow P_4$ requires an energy transfer ~ 0.9 eV, as also shown by the vertical green arrow in Figure 3b. This scattering creates a gapped response peak in the orbital excitations at $k \simeq 0$ and $\omega \simeq 0.9$ eV (Fig. 2e and 4a). The charge gap of orbital c in $N^c(k, \omega)$ can also be understood via the scattering between points P_1 and P_4 of the density-of-states, also shown by vertical green arrows in Fig. 3b. Additionally, the gapless continuum in $L^z(k, \omega)$ is very similar to the

itinerant charge excitations, $N^{a/b}(k, \omega)$, because only the (almost degenerate) itinerant orbitals are involved in the calculations of $L^z(k, \omega)$.

FM insulator — To identify features of orbital excitations in the block OSMP that are unique, we also show k -resolved orbital excitations in the FM insulator known to exist at $U/W = 4$ [24], see Figs. 2g and 2h. Both $L^{x/y}(k, \omega)$ and $L^z(k, \omega)$ display sharper excitations in the FM phase. Additionally, $L^z(k, \omega)$ is gapless with a $\omega \simeq 0$ peak at $k = \pi$, implying quasi-long-range antiferro-orbital order in the ground state, as discussed before [25]. In fact, the $L^z(k, \omega)$ of the FM phase resembles the $S(k, \omega)$ of the spin-1/2 Heisenberg chain with a two-spinon continuum. By analogy, we conjecture that the $L^z(k, \omega)$ of the FM phase may denote the existence of fractionalized orbital excitations [41].

Discussion — Our main result is in Fig. 4, where we compare the calculated orbital dynamical response vs. RIXS Fe- L_3 edge experimental data for BaFe₂Se₃ at zero-momentum transfer [20]. Relating the full RIXS intensity to dynamical structure factors is not easy [30, 42]: for example, for the single-band Hubbard model the RIXS intensity can be directly related to dynamical structure factors only in limiting cases. However, the dynamical response functions can still provide insights into the dominant features and energy scales of RIXS experiments.

At zero energy transfer, there is an “elastic” peak commonly observed in RIXS experiments. To identify the unique features of orbital excitations in the Block OSMP ($U/W = 0.8$), we also present results for the PM ($U/W = 0.04$) and FM ($U/W = 4$) phases. Over-

all, we find a close agreement between our dynamical spectra in the block OSMP at $k \simeq 0$ with the two-peak structure observed in experiments, involving localized dd excitations of the iron $3d$ orbitals. Moreover, the two-peak structure is clearly present only in the block OSMP (Fig. 4a) and not in the PM or FM phases (Figs. 4b or 4c), although there is a precursor in the PM phase. Our model indicates that the experimentally observed peaks represent excitations between localized d_{xy} and itinerant $d_{xz/yz}$ orbitals. They are gapped with an activation energy $0.7-0.9$ eV in the calculations, and $\sim 0.35-0.45$ eV in the experiments (transitions involving e_g orbitals, outside our model, should appear at higher energies). This gap difference in absolute numbers could be fixed by small changes in our model parameters (or by using ladders instead of chains). In addition in the real samples there is broadening due to phonons and non-crystallinity effects that make the gap difficult to define accurately. *Our results suggests that the experimentally observed gap is not a conventional semi-conducting gap, but instead originates from the inter-orbital excitations of an OSMP.* Figure 4a shows that peak A occurs at approximately 0.9 eV, for the zero momentum transfer, as a result of vertical ($\Delta k = 0$) scattering across E_F from the itinerant $d_{xz/yz}$ orbitals to the d_{xy} Mott orbital (Fig. 3b, $P_2 \rightarrow P_4$). The shoulder/peak labeled as B represents scattering from the localized d_{xy} band below E_F to the itinerant hole pocket bands $d_{xz/yz}$ above E_F , with zero momentum transfer $k/\pi = 0$ (Fig. 3b, $P_1 \rightarrow P_3$). These peaks can not be characterized within a simple weak-coupling framework. In fact, measuring real-space orbital correlations at various energy transfers [32] we also find that the peak A of the block OSMP represents a final state with ferro-orbital ordering, while B represents a final state with short-range anti-ferro orbital ordering.

The orbital d_{xy} charge excitations in our calculations generate a response at $\omega = 1.4$ eV of intensity ~ 100 times smaller than the orbital excitations (Figs. 2c-2f). This is because local charge fluctuations are suppressed significantly in the Mott orbital. Additionally, the features in $N^{a/b}(k, \omega)$ and $L^z(k, \omega)$ originate from itinerant carriers that are sensitive to the incident x-ray energy ($\hbar\omega_{in}$) of the RIXS experiments. It is known that localized excitations do not shift with $\hbar\omega_{in}$, while itinerant carriers produce a response that shifts linearly with $\hbar\omega_{in}$, becoming part of the fluorescence at large $\hbar\omega_{in}$ [43]. Therefore, the $L^z(k, \omega)$ peak at the low-energy transfer ω (Fig. 4a, dashed) will shift with the incident energy. In fact, RIXS experiment on BaFe_2Se_3 also find (fluorescence) peaks that shift with incident energy and merge with the localized excitations (A and B of Fig. 4a), suggesting the existence of both localized and itinerant degrees of freedom at the experimental low temperature, as also found for the OSMP regime in our calculations.

Conclusions — We calculated the momentum-resolved orbital and charge dynamics of an orbital-selective Mott

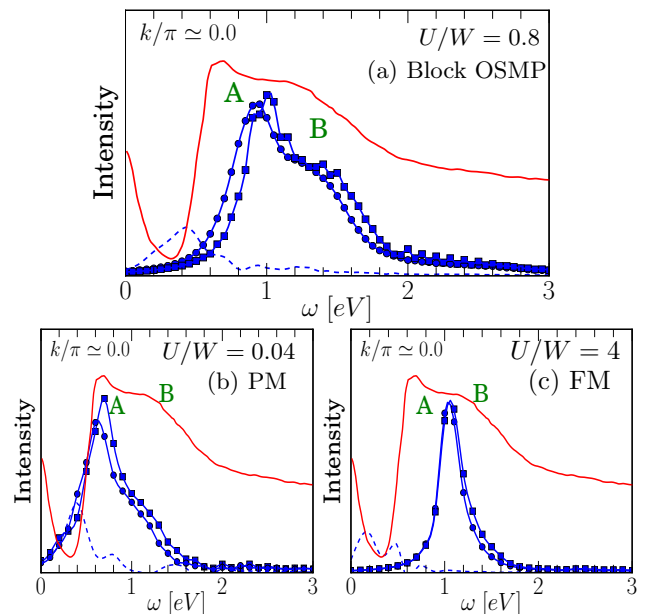


FIG. 4. (color online) Orbital excitations spectra (blue) at zero-momentum transfer at (a) $U/W = 0.8$ (block OSMP), (b) $U/W = 0.04$ (PM phase), and (c) $U/W = 4$ (FM insulator) using DMRG and 16 sites. For comparison, each panel shows the experimental RIXS data (red) at the Fe- L_3 edge [20], where peaks A and B are dd excitations. Peak A is caused by the $P_2 \rightarrow P_4$ excitations of Fig. 3a, while the subdominant peak B seems caused by the $P_1 \rightarrow P_3$ excitations of the same figure.

phase using the three t_{2g} orbitals, and compared our results to the available RIXS data for BaFe_2Se_3 at zero momentum transfer [20]. We find localized dd excitations that produce particular peaks A and B very similar to those observed experimentally, providing theoretical support for the notion that BaFe_2Se_3 is an orbital-selective Mott insulator. Moreover, we predict the k -resolved charge and orbital dynamical spectra that can be measured by RIXS in the future. Recent RIXS experiments display a very similar response for BaFe_2Se_3 and BaFe_2S_3 , implying that an orbital-selective phase is present in the BaFe_2S_3 high-pressure superconductor as well [1, 44]. We encourage the measurement of the band structure and density-of-states of these materials using angle-resolved photoemission and scanning tunneling microscopy, to confirm our predicted band(s) crossing of the Fermi surface and Mott like band(s) below the Fermi surface. We also encourage future k -resolved RIXS measurements for BaFe_2Se_3 and BaFe_2S_3 compounds.

Acknowledgments — We thank C. Monney and T. Schmitt for providing a copy of the experimental data shown in Fig. 4. N. D. P., A. N., A. M., and E. D. were supported by the U.S. Department of Energy (DOE), Office of Science, Basic Energy Sciences (BES), Materials Science and Engineering Division. G. A. and S. J. were supported by the Scientific Discovery through Advanced Computing (SciDAC) program funded by the U.S. De-

partment of Energy, Office of Science, Advanced Scientific Computing Research and Basic Energy Sciences, Division of Materials Sciences and Engineering. N. D. P. was also partially supported by the National Science Foundation Grant No. DMR-1404375. Part of this work was conducted at the Center for Nanophase Materials Sciences, sponsored by the Scientific User Facilities Division (SUFD), BES, DOE, under contract with UT-Battelle. Computer time provided in part by resources supported by the University of Tennessee and Oak Ridge National Laboratory Joint Institute for Computational Sciences.

-
- [1] H. Takahashi, A. Sugimoto, Y. Nambu, T. Yamauchi, Y. Hirata, T. Kawakami, M. Avdeev, K. Matsubayashi, F. Du, C. Kawashima, et al., *Nature Materials* **14**, 1008 (2015), URL <http://dx.doi.org/10.1038/nmat4351>.
- [2] T. Yamauchi, Y. Hirata, Y. Ueda, and K. Ohgushi, *Phys. Rev. Lett.* **115**, 246402 (2015), URL <https://link.aps.org/doi/10.1103/PhysRevLett.115.246402>.
- [3] J. Ying, H. Lei, C. Petrovic, Y. Xiao, and V. V. Struzhkin, *Phys. Rev. B* **95**, 241109 (2017), URL <https://link.aps.org/doi/10.1103/PhysRevB.95.241109>.
Y. Zhang, L.-F. Lin, J.-J. Zhang, E. Dagotto, and S. Dong, *Phys. Rev. B* **97**, 045119 (2018), URL <https://link.aps.org/doi/10.1103/PhysRevB.97.045119>.
- [4] D. Basov and A. V. Chubukov, *Nature Physics* **7**, 272 (2011), URL <https://www.nature.com/articles/nphys1975>.
R. M. Fernandes and A. V. Chubukov, *Reports on Progress in Physics* **80**, 014503 (2017), URL <http://stacks.iop.org/0034-4885/80/i=1/a=014503>.
- [5] P. Dai, J. Hu, and E. Dagotto, *Nature Physics* **85**, 709 (2012), URL <http://dx.doi.org/10.1038/nphys2438>.
- [6] E. Dagotto, *Rev. Mod. Phys.* **85**, 849 (2013), URL <https://link.aps.org/doi/10.1103/RevModPhys.85.849>.
- [7] S. R. White, *Phys. Rev. Lett.* **69**, 2863 (1992), URL <https://link.aps.org/doi/10.1103/PhysRevLett.69.2863>.
- [8] U. Schollwöck, *Rev. Mod. Phys.* **77**, 259 (2005), URL <https://link.aps.org/doi/10.1103/RevModPhys.77.259>.
- [9] S. R. White, *Phys. Rev. B* **72**, 180403 (2005), URL <https://link.aps.org/doi/10.1103/PhysRevB.72.180403>.
- [10] S. R. White, *Phys. Rev. Lett.* **77**, 3633 (1996), URL <https://link.aps.org/doi/10.1103/PhysRevLett.77.3633>.
- [11] G. Alvarez, *Computer Physics Communications* **180**, 1572 (2009), URL <https://doi.org/10.1016/j.cpc.2009.02.016>.
- [12] N. D. Patel, A. Nocera, G. Alvarez, R. Arita, A. Moreo, and E. Dagotto, *Phys. Rev. B* **94**, 075119 (2016), URL <https://link.aps.org/doi/10.1103/PhysRevB.94.075119>.
- [13] Y. Nambu, K. Ohgushi, S. Suzuki, F. Du, M. Avdeev, Y. Uwatoko, K. Munakata, H. Fukazawa, S. Chi, Y. Ueda, et al., *Phys. Rev. B* **85**, 064413 (2012), URL <https://link.aps.org/doi/10.1103/PhysRevB.85.064413>.
- [14] N. D. Patel, A. Nocera, G. Alvarez, A. Moreo, and E. Dagotto, *Phys. Rev. B* **96**, 024520 (2017), URL <https://link.aps.org/doi/10.1103/PhysRevB.96.024520>.
- [15] J. M. Caron, J. R. Neilson, D. C. Miller, A. Llobet, and T. M. McQueen, *Phys. Rev. B* **84**, 180409 (2011), URL <https://link.aps.org/doi/10.1103/PhysRevB.84.180409>.
- [16] H. Lei, H. Ryu, A. I. Frenkel, and C. Petrovic, *Phys. Rev. B* **84**, 214511 (2011), URL <https://link.aps.org/doi/10.1103/PhysRevB.84.214511>.
- [17] J. M. Caron, J. R. Neilson, D. C. Miller, K. Arpino, A. Llobet, and T. M. McQueen, *Phys. Rev. B* **85**, 180405 (2012), URL <https://link.aps.org/doi/10.1103/PhysRevB.85.180405>.
- [18] Q. Luo, A. Nicholson, J. Rincón, S. Liang, J. Riera, G. Alvarez, L. Wang, W. Ku, G. D. Samolyuk, A. Moreo, et al., *Phys. Rev. B* **87**, 024404 (2013), URL <https://link.aps.org/doi/10.1103/PhysRevB.87.024404>.
- [19] M. Mourigal, S. Wu, M. B. Stone, J. R. Neilson, J. M. Caron, T. M. McQueen, and C. L. Broholm, *Phys. Rev. Lett.* **115**, 047401 (2015), URL <https://link.aps.org/doi/10.1103/PhysRevLett.115.047401>.
- [20] C. Monney, A. Uldry, K. J. Zhou, A. Krzton-Maziopa, E. Pomjakushina, V. N. Strocov, B. Delley, and T. Schmitt, *Phys. Rev. B* **88**, 165103 (2013), URL <https://link.aps.org/doi/10.1103/PhysRevB.88.165103>.
- [21] D. Ootsuki, N. L. Saini, F. Du, Y. Hirata, K. Ohgushi, Y. Ueda, and T. Mizokawa, *Phys. Rev. B* **91**, 014505 (2015), URL <https://link.aps.org/doi/10.1103/PhysRevB.91.014505>.
- [22] A. Georges, L. de' Medici, and J. Mravlje, *Annual Review of Condensed Matter Physics* **4**, 137 (2013), and references therein, URL <https://doi.org/10.1146/annurev-conmatphys-020911-125045>.
- [23] R. Yu and Q. Si, *Phys. Rev. Lett.* **110**, 146402 (2013), URL <https://link.aps.org/doi/10.1103/PhysRevLett.110.146402>.
- [24] J. Rincón, A. Moreo, G. Alvarez, and E. Dagotto, *Phys. Rev. Lett.* **112**, 106405 (2014), URL <https://link.aps.org/doi/10.1103/PhysRevLett.112.106405>.
- [25] S. Li, N. Kaushal, Y. Wang, Y. Tang, G. Alvarez, A. Nocera, T. A. Maier, E. Dagotto, and S. Johnston, *Phys. Rev. B* **94**, 235126 (2016), URL <https://link.aps.org/doi/10.1103/PhysRevB.94.235126>.
- [26] J. Herbrych, N. Kaushal, A. Nocera, G. Alvarez, A. Moreo, and E. Dagotto, *ArXiv:1804.01959* (2018), URL <https://arxiv.org/abs/1804.01959>.
- [27] L. J. P. Ament, M. van Veenendaal, T. P. Devereaux, J. P. Hill, and J. van den Brink, *Rev. Mod. Phys.* **83**, 705 (2011), URL <https://link.aps.org/doi/10.1103/RevModPhys.83.705>.
- [28] K. Wohlfeld, S. Nishimoto, M. W. Haverkort, and J. van den Brink, *Phys. Rev. B* **88**, 195138 (2013), URL <https://link.aps.org/doi/10.1103/PhysRevB.88.195138>.
- [29] P. Marra, K. Wohlfeld, and J. van den Brink, *Phys. Rev. Lett.* **109**, 117401 (2012), URL <https://link.aps.org/doi/10.1103/PhysRevLett.109.117401>.
- [30] C. Jia, E. Nowadnick, K. Wohlfeld, Y. Kung, C.-C. Chen, S. Johnston, T. Tohyama, B. Moritz, and T. Devereaux, *Nature Communications* **5**, 3314 (2014), URL <https://>

- www.nature.com/articles/ncomms4314.
- [31] S. Johnston, C. Monney, V. Bisogni, Z. K.-J., R. Kraus, G. Behr, V. N. Strocov, J. Málek, S.-L. Drechsler, J. Geck, et al., Nature Communications **7**, 10563 (2016), URL <https://www.nature.com/articles/ncomms10563>.
- [32] The supplementary material at [URL will be inserted by publisher] contains details of the definition of operators, observables, additional numerical results, and input files.
- [33] K. Haule and G. Kotliar, New Journal of Physics **11**, 025021 (2009), URL <http://stacks.iop.org/1367-2630/11/i=2/a=025021>.
- [34] Q. Luo, G. Martins, D.-X. Yao, M. Daghofer, R. Yu, A. Moreo, and E. Dagotto, Phys. Rev. B **82**, 104508 (2010), URL <https://link.aps.org/doi/10.1103/PhysRevB.82.104508>.
- [35] A. Nocera and G. Alvarez, Phys. Rev. E **94**, 053308 (2016), URL <https://link.aps.org/doi/10.1103/PhysRevE.94.053308>.
- [36] T. D. Kühner and S. R. White, Phys. Rev. B **60**, 335 (1999), URL <https://link.aps.org/doi/10.1103/PhysRevB.60.335>.
- [37] For an analysis of the full phase diagram varying the electronic density, and for a discussion of several OSMP states see J. Rincón, A. Moreo, G. Alvarez, and E. Dagotto, Phys. Rev. B **90**, 241105 (2014), URL <https://link.aps.org/doi/10.1103/PhysRevB.90.241105>.
- [38] Note that the finite weight at μ in the c orbital is due to broadening.
- [39] L. de' Medici, ArXiv:1707.03282 (2017), URL <https://arxiv.org/abs/1707.03282>.
- [40] A. Nocera, Y. Wang, N. D. Patel, G. Alvarez, T. A. Maier, E. Dagotto, and S. Johnston, Phys. Rev. B **97**, 195156 (2018), URL <https://link.aps.org/doi/10.1103/PhysRevB.97.195156>.
- [41] J. Schlappa, K. Wohlfeld, K. Zhou, M. Mourigal, M. Haverkort, V. Strocov, L. Hozoi, C. Monney, S. Nishimoto, S. Singh, et al., Nature **485**, 82 (2012), URL <https://www.nature.com/articles/nature10974>.
- [42] C. Jia, K. Wohlfeld, Y. Wang, B. Moritz, and T. P. Devereaux, Phys. Rev. X **6**, 021020 (2016), URL <https://link.aps.org/doi/10.1103/PhysRevX.6.021020>.
- [43] V. Bisogni, S. Catalano, R. J. Green, M. Gibert, R. Scherwitsl, Y. Huang, V. N. Strocov, P. Zubko, S. Balandeh, J.-M. Triscone, et al., Nature Communications **7**, 13017 (2016), URL <http://dx.doi.org/10.1038/ncomms13017>.
- [44] K. Takubo, Y. Yokoyama, H. Wadati, S. Iwasaki, T. Mizokawa, T. Boyko, R. Sutarto, F. He, K. Hashizume, S. Imaizumi, et al., Phys. Rev. B **96**, 115157 (2017), URL <https://link.aps.org/doi/10.1103/PhysRevB.96.115157>.
-

Supplemental: Orbital and Charge Excitations as Fingerprints of an Orbital-Selective Mott Phase in the Block Magnetic State of BaFe₂Se₃

OPERATORS AND OBSERVABLES

In this section, we define all the operators that are used in the main text:

$$\begin{aligned}
 n_{i\gamma\sigma} &= c_{i\gamma\sigma}^\dagger c_{i\gamma\sigma}, \\
 n_{i\gamma} &= n_{i\gamma\uparrow} + n_{i\gamma\downarrow}, \\
 S_{i\gamma}^\kappa &= \frac{1}{2} \sum_{\sigma,\sigma'} c_{i\gamma\sigma}^\dagger \sigma_{\sigma\sigma'}^\kappa c_{i\gamma\sigma'}, \\
 P_{i\gamma} &= c_{i\gamma\uparrow} c_{i\gamma\downarrow},
 \end{aligned} \tag{S1}$$

where γ is the orbital index, σ and σ' are the spin index, and σ^κ are the Pauli matrices with $\kappa = \{x, y, z\}$ being Cartesian components. The average occupation and charge fluctuations (Fig.1 of main text) are defined as

$$\begin{aligned}
 \langle n_\gamma \rangle &= \frac{1}{L} \sum_{i,\sigma} n_{i\gamma\sigma}, \\
 \langle \delta N_\gamma^2 \rangle &= \frac{1}{L} \sum_i \langle n_{i\gamma} n_{i\gamma} \rangle - \langle n_{i\gamma} \rangle \langle n_{i\gamma} \rangle,
 \end{aligned} \tag{S2}$$

where L is the number of sites in the lattice. The static spin-spin correlations (inset of Fig. 1) is calculated using

$$S(k) = \frac{1}{L^2} \sum_{i,j} e^{-ik(i-j)} \langle \mathbf{S}_i \cdot \mathbf{S}_j \rangle, \tag{S3}$$

where $\mathbf{S}_i = \sum_\gamma \mathbf{S}_{i\gamma}$. In this supplemental, we also show results for n_k^γ defined as

$$\begin{aligned}
 c_{j\gamma} &= c_{j\gamma\uparrow} + c_{j\gamma\downarrow}, \\
 n^\gamma(k) &= n_k^\gamma = \frac{1}{L^2} \sum_{i,j} e^{-ik(i-j)} \langle c_{i\gamma}^\dagger c_{j\gamma} \rangle.
 \end{aligned} \tag{S4}$$

Spectral functions and sum rules

To characterize the OSMP, the dynamical response functions (shown below) are calculated using DMRG

$$O(i, j, \omega) = \frac{-1}{\pi} \text{Im} \left[\langle \psi_0 | O_i^\dagger \frac{1}{\omega - H + E_g + i\eta} O_j | \psi_0 \rangle \right], \tag{S5}$$

where the local operator O_i can represent any degree of freedom of the model. In general, these functions are Fourier transformed into the crystal momentum domain to calculate the momentum-energy resolved spectra that is relevant to experiments:

$$O(k, \omega) = \frac{1}{L^2} \sum_{i,j} e^{-ik(i-j)} O(i, j, \omega). \tag{S6}$$

Note that within DMRG, the site j is fixed to the center of the lattice ($d = L/2 - 1$) to reduce the edge effects and computational cost, and therefore the modified Fourier transform becomes

$$O(k, \omega) = \frac{1}{L} \sum_i e^{-ik(i-d)} O(i, d, \omega). \tag{S7}$$

Additionally, we use open boundary conditions in the DMRG simulation and therefore the quasi crystal-momenta are defined as

$$k = \frac{\pi n}{L+1} \quad \text{where } n = 1, 2, \dots, L. \tag{S8}$$

ORBITAL OPERATORS

The dominant orbitals of an iron atom in iron-based superconductors are the five $3d$ orbitals, corresponding to well-known $L = 2$ orbital angular momenta. The corresponding operators $\{L_x, L_y, L_z\}$ are written in the basis of $L_z = \{-2, -1, 0, 1, 2\}$, forming 5×5 matrices:

$$\begin{aligned}
 L_x &= \frac{1}{2} \begin{bmatrix} 0 & 2 & 0 & 0 & 0 \\ 2 & 0 & \sqrt{6} & 0 & 0 \\ 0 & \sqrt{6} & 0 & \sqrt{6} & 0 \\ 0 & 0 & \sqrt{6} & 0 & 2 \\ 0 & 0 & 0 & 2 & 0 \end{bmatrix} \\
 L_y &= \frac{-i}{2} \begin{bmatrix} 0 & 2 & 0 & 0 & 0 \\ -2 & 0 & \sqrt{6} & 0 & 0 \\ 0 & -\sqrt{6} & 0 & \sqrt{6} & 0 \\ 0 & 0 & -\sqrt{6} & 0 & 2 \\ 0 & 0 & 0 & -2 & 0 \end{bmatrix} \\
 L_z &= \begin{bmatrix} 2 & 0 & 0 & 0 & 0 \\ 0 & 1 & 0 & 0 & 0 \\ 0 & 0 & 0 & 0 & 0 \\ 0 & 0 & 0 & -1 & 0 \\ 0 & 0 & 0 & 0 & -2 \end{bmatrix}
 \end{aligned}$$

DMRG is a real-space algorithm, and therefore we must write these matrices in the orbital basis using the transformation

$$\begin{aligned}
 |-2\rangle &= \frac{1}{\sqrt{2}} (|x^2 - y^2\rangle - i|xy\rangle), \\
 |-1\rangle &= \frac{1}{\sqrt{2}} (|xz\rangle - i|yz\rangle), \\
 |0\rangle &= |z^2\rangle, \\
 |1\rangle &= \frac{-1}{\sqrt{2}} (|xz\rangle + i|yz\rangle), \\
 |2\rangle &= \frac{1}{\sqrt{2}} (|x^2 - y^2\rangle + i|xy\rangle),
 \end{aligned} \tag{S9}$$

where $\{|x^2 - y^2\rangle, |z^2\rangle, |xz\rangle, |yz\rangle, |xy\rangle\}$ are the five iron $3d$ orbitals. The operators $\{L_x, L_y, L_z\}$ represented in the orbital basis are:

$$L_x = \frac{i}{2} \begin{bmatrix} 0 & 0 & 0 & 1 & 0 \\ 0 & 0 & 0 & \sqrt{3} & 0 \\ 0 & 0 & 0 & 0 & 1 \\ -1 & -\sqrt{3} & 0 & 0 & 0 \\ 0 & 0 & -1 & 0 & 0 \end{bmatrix}$$

$$L_y = \frac{i}{2} \begin{bmatrix} 0 & 0 & -1 & 0 & 0 \\ 0 & 0 & \sqrt{3} & 0 & 0 \\ 1 & -\sqrt{3} & 0 & 0 & 0 \\ 0 & 0 & 0 & 0 & 1 \\ 0 & 0 & 0 & -1 & 0 \end{bmatrix}$$

$$L_z = i \begin{bmatrix} 0 & 0 & 0 & 0 & 2 \\ 0 & 0 & 0 & 0 & 0 \\ 0 & 0 & 0 & 1 & 0 \\ 0 & 0 & -1 & 0 & 0 \\ -2 & 0 & 0 & 0 & 0 \end{bmatrix}.$$

In the main text, we employ the iron t_{2g} orbitals, *i.e.*, we drop the contribution from $|x^2 - y^2\rangle, |z^2\rangle$ orbitals. After this approximation, we obtain the local orbital angular momentum operators used in the main text (site index understood)

$$\begin{aligned} L^x &= i(c_{xz}^\dagger c_{xy} - c_{xy}^\dagger c_{xz}), \\ L^y &= i(c_{yz}^\dagger c_{xy} - c_{xy}^\dagger c_{yz}), \\ L^z &= i(c_{xz}^\dagger c_{yz} - c_{yz}^\dagger c_{xz}). \end{aligned} \quad (\text{S10})$$

ADDITIONAL RESULTS

In this section, we show tests performed to ensure the quality of the presented results. We first show $n^\gamma(k)$ that is in agreement with previous studies with a similar model [25]. A significant change in $n^{a/b}(k)$ indicates metallic behavior of these orbitals. On the contrary, $n^c(k)$ shows little variation in k that is associated with a gapped orbital c .

Furthermore, all spectral quantities defined by equations S5 and S6 must satisfy a sum rule. In general, it can be shown that integrating the spectral function over momentum k and energy ω gives a quantity related to a unique static observable. As an example, we use the single-particle spectral function $A^c(k, \omega)$ of orbital c below (above) the Fermi energy (E_F) representing the filled (unfilled) electron (hole) states. The electron and hole

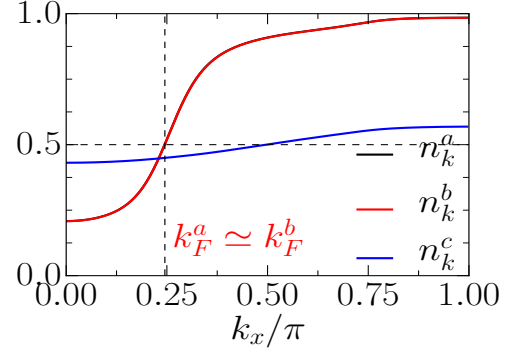


FIG. S1. (color online) $n^\gamma(k)$ for the Block OSMP ($U/W = 0.8$) using a 32 sites chain. The largest increase in $n^\gamma(k)$ of the itinerant orbitals a (black) and b (red) occurs at $k/\pi \simeq 0.25$, *i.e.* the Fermi momentum. Note that results for a and b are almost identical, thus indistinguishable in the figure. $n^c(k)$ of the localized orbital c has only a slight variation in k , suggesting a gap in the single-particle states of orbital c . These results are in agreement with previous studies using Quantum Monte Carlo [25].

components of $A^c(k, \omega)$ are defined as

$$\begin{aligned} A_e^c(k, \omega) &= \frac{-1}{\pi L^2} \times \\ &\sum_{i,j} \text{Im} \left[\langle \psi_0 | c_{ic}^\dagger \frac{1}{\omega - H + E_g + i\eta} c_{jc} | \psi_0 \rangle \right] e^{-ik(i-j)}, \\ A_h^c(k, \omega) &= \frac{-1}{\pi L^2} \times \\ &\sum_{i,j} \text{Im} \left[\langle \psi_0 | c_{ic} \frac{1}{\omega + H + E_g + i\eta} c_{jc}^\dagger | \psi_0 \rangle \right] e^{-ik(i-j)}, \end{aligned} \quad (\text{S11})$$

where c is the orbital index and $c_{jc} = c_{jc\uparrow} + c_{jc\downarrow}$. To obtain the sum rule of this quantity, we first sum over the momentum k . This sum simply results in $L\delta_{i,j}$, giving us the local response that is the single-particle density of states,

$$\begin{aligned} A_e^c(\omega) &= -\frac{1}{\pi L} \sum_i \text{Im} \left[\langle \psi_0 | c_{ic}^\dagger \frac{1}{\omega - H + E_g + i\eta} c_{ic} | \psi_0 \rangle \right], \\ A_h^c(\omega) &= -\frac{1}{\pi L} \sum_i \text{Im} \left[\langle \psi_0 | c_{ic} \frac{1}{\omega + H + E_g + i\eta} c_{ic}^\dagger | \psi_0 \rangle \right], \end{aligned} \quad (\text{S12})$$

shown in Figure S2. Further integration over ω of the imaginary part (Lorentzian poles) of the electron (hole) part simply gives the total electron (hole) density of orbital c :

$$\begin{aligned} n_e^c &= \frac{1}{L} \sum_i \langle \psi_0 | c_i^\dagger c_i | \psi_0 \rangle, \\ n_h^c &= \frac{1}{L} \sum_i \langle \psi_0 | c_i c_i^\dagger | \psi_0 \rangle. \end{aligned} \quad (\text{S13})$$

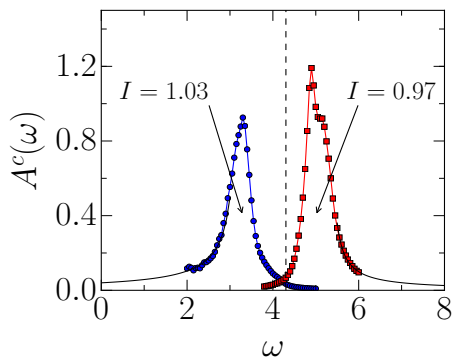


FIG. S2. (color online) Density of states of the Mott orbital c , calculated using the electron (A_e^c , blue) and hole (A_h^c , red) components, employing 24 sites, $\Delta\omega = 0.05$, and $\eta = 0.1$. The vertical grey line represents the Fermi energy $E_F \simeq 4.3$ eV. The tails of the density of states are fitted in order to account for the missing tail weights. $I \simeq 1$ is the integrated value of the electron and hole part of the density of states which is respectively equal to the average local electron and hole occupations.

This is explicitly done within our calculations by integrating over the density of states (Fig. S2). The integration of the electron (blue curve) and hole (red curve) portions lead to approximately 1.0 that is consistent, within the accuracy of our results, with calculations of the local density from the ground-state. Note that a singly occupied orbital is one of the characteristics of a Mott insulator.

We also performed finite-size scaling on the density of states at the Fermi energy $E_F \simeq 4.3$ eV. Figure S3 shows that the $L \rightarrow \infty$ extrapolated quasi-particle weight, $A(\omega = E_F)$, of orbital c is an order of magnitude smaller than the almost degenerate orbitals a and b . The near zero weight of orbital c at the Fermi energy is consistent with a Mott phase, providing further evidence of the presence of an OSMP as the ground-state.

In Fig. 4 of the main text, we demonstrated that the peaks found in the orbital excitations of the OSMP are similar to the peaks found in the RIXS experiment on BaFe_2Se_3 . We also provided a rationalization of the peak positions using single-particle spectra that is renormalized by the interactions. Here, we again emphasize that the presence of a Mott insulating orbital imply that weak coupling arguments are not sufficient to understand the orbital excitations of an OSMP. To understand better the states at peak positions A and B (Fig. 4), we show real-space orbital correlations vs. energy transfer in Fig. S4. In the block OSMP, the A peak presents positive $L_{x/y}$ correlations up to 4^{th} nearest neighbor in real space, while peak B has negative $L_{x/y}$ correlations only up to the nearest neighbor. In Fig. S4a, we explicitly show that the peak A of the block OSMP represents states

with ferro-orbital ordering, while B represents states with

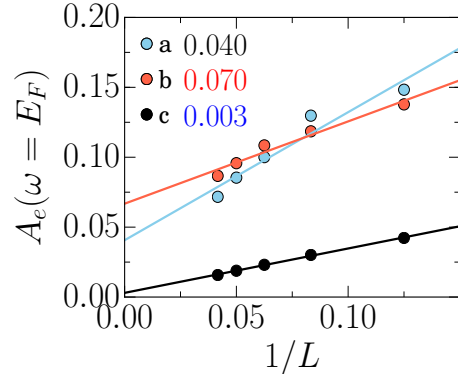


FIG. S3. (color online) Finite-size scaling of the orbital-resolved electron part of the density of states at the Fermi energy (E_F). The quasi-particle weight of the Mott orbital approaches 0 (more accurately, 0.003) with increasing system size while the weight remains finite for the itinerant orbitals (0.04 and 0.07). Note that $A_e(E_F)$ of the itinerant orbitals a and b is an order magnitude larger than the Mott orbital c , further emphasizing that orbital c is a Mott insulator.

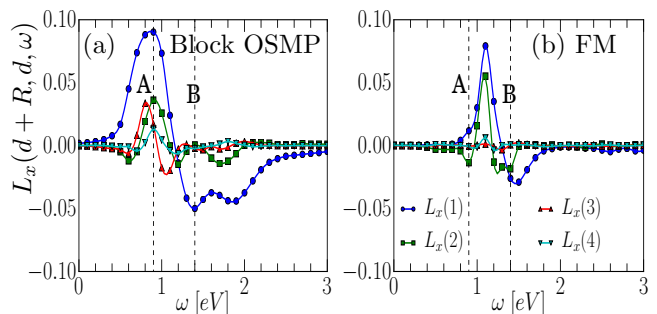


FIG. S4. (color online) Real-space $L_x(d + R, d, \omega)$ [using $O_i = L_{d+R}^x$ and $O_j = L_d^x$ in Eq.S5] vs. ω with a fixed center site $d = 8$ on a 16-sites three-orbital chain in the (a) block OSMP ($U/W = 0.8$) and (b) FM insulator ($U/W = 4$) phases. Labels A and B (vertical dashed line) show the peak positions labels in Fig. 4 of the main text. Overall negative (positive) response denote local antiferro (ferro) orbital ordering.

short-range anti-ferro orbital ordering. Similar features are also present for the FM case (Fig. S4b) but positive correlations (at $\omega \simeq 1.1$) persist only up to the 2^{nd} nearest neighbor, while antiferro-orbital tendencies (negative correlation - peak B) are significantly suppressed.

REPRODUCING DATA USING DMRG++

The full open source code, sample inputs, and corresponding computational details can be found at <https://github.com/g1257/papers/86/>.